# Mechanism of the Trickle-to-Pulse Flow Transition in Fixed-Bed Reactors

**Laura D. Anadon, Andrew J. Sederman, and Lynn F. Gladden**
Dept. of Chemical Engineering, University of Cambridge, Pembroke Street, Cambridge CB2 3RA, U.K.

*DOI 10.1002/aic.10737*
*Published online December 6, 2005 in Wiley InterScience (www.interscience.wiley.com).*

*The formation of local instabilities, identified as isolated pulsing events, in the gas-liquid distribution within a trickle-bed reactor is shown to be central to the mechanism of the hydrodynamic transition from trickle-to-pulsing flow. The evolution of these instabilities as the bed moves through the transition is imaged in 3-D using ultrafast magnetic resonance imaging (MRI). The reactor was of internal dia. 43 mm and packed with cylindrical packing elements of length and diameter 3 mm, operating under conditions of air-water, cocurrent downflow. Superficial gas and liquid velocities in the range 25–300 and 0.9–13.0 mm* $s^{-1}$*, respectively, were used. For a given gas velocity, the transition point is defined to be the liquid velocity at which the maximum number of isolated pulses occurs. The transition point determined using this approach is critically compared with the predictions of existing correlations and theoretical models.* © 2005 American Institute of Chemical Engineers *AIChE J,* 52: 1522–1532, 2006
*Keywords: trickle-bed reactor, hydrodynamic transition, magnetic resonance imaging, pulsing regime, two-phase flow*

## Introduction

Trickle-bed reactors consist of a fixed bed of catalyst particles, contacted by gas-liquid two-phase flow, with cocurrent downflow as the most common mode of operation. Trickle beds are the most frequently used type of gas-liquid-solid reactor[1] with widespread applications in the petroleum, petrochemical and chemical industries, as well as increasing applications in biochemical and electrochemical processing and waste (gas or liquid) treatment. Typical reactions carried out in trickle-bed reactors involve hydrogenations, oxidations and various types of hydrotreatments, for example, hydrocracking, hydrodenitrogenation and hydrodesulfurization.

For the case of nonfoaming systems, trickle-bed reactors can be operated in various flow regimes depending on the fluid properties and flow rates, and the packing characteristics.[2] These flow regimes are commonly divided into a low interaction regime (trickle flow), where the flow of one phase is not affected by the flow of the other one, and a high interaction regime (including pulsing, bubble and spray flow), where interactions between the two phases do affect the flow pattern.[3-5] It is well known that the flow regime within a given trickle-bed reactor will influence characteristics, such as phase holdups, power consumption and mass-transfer fluxes,[6,7] and, hence, conversion and selectivity. Therefore, successful modeling of trickle-bed reactors requires precise tools for the identification of the flow pattern to be expected for a specified set of operating conditions. In this article we demonstrate the power of ultrafast three-dimensional (3-D) MRI to provide such detailed information.

The transition between the trickle and pulsing flow regimes has attracted particular attention for two reasons. First, many industrial trickle-bed reactors are operated either in trickle flow, in pulsing flow or somewhere near the transition.[5,8] Second, it is vital to gain an improved understanding of the two-phase fluid dynamics and transport processes in pore networks both at particle- and reactor-scale to achieve successful process scaleup.[1,9,10] Consequently, numerous empirical, semiempirical and theoretical models aiming to predict the transition conditions have been proposed in the litera-

Correspondence concerning this article should be addressed to L. F. Gladden at Gladden@cheng.cam.ac.uk.

ture.[1,4,7,11-13] Only a brief overview of the most relevant experimental and theoretical approaches is given here.

The earliest approach predicted the transition based on flow maps and correlations obtained empirically by observing the flow pattern inside the trickle bed through transparent walls.[14,15] For example, Blok et al.[15] observed that the transition occurred at a constant value of the real velocity, as defined by their own empirical correlation to determine the liquid holdup, and proposed a constant Froude number as the criterion for the transition. The inevitable shortcoming of such approaches is that one is relying on the observation of hydrodynamics close to the walls of the reactor as being representative of the global bed behavior which will not necessarily be the case. The most recent empirical approach is that reported by Larachi et al.[7] who derived a correlation using a feed-forward neural network approach, based on a database compiled from a detailed survey of all trickle-to-pulse flow transition data published between 1964 and 1994.

The more theoretical modeling approaches fall into two groups. The first group relates the bed-scale transition to phenomena occurring at the pore scale, we will refer to these as "microscopic" models. In this context a "pore" refers to an element of the channel structure within the bed of a length scale typical of the packing elements comprising the bed. For instance, Sicardi et al.[11] suggested that a trickle bed may be considered as consisting of constricted parallel channels, and that inception of pulse flow occurs when large waves on the liquid surface occlude the constrictions. Along a similar theme, Ng[16] postulated that pulsing occurs when growing liquid films first block the constrictions between particles. Holub et al.[4] suggested that the transition was caused by the loss of stability of the laminar liquid film, as predicted by Kapitza's criterion[17] for the onset of interfacial waves, and included an empirical correction to account for the trends in the transition as a function of Galileo number and the dimensionless liquid phase pressure drop. Although these models were based on physical phenomena, in the absence of experimental determination of the required input data, they still rely, to some extent, on use of empirical correlations. For example, Ng's model requires a value for the liquid holdup at the onset of pulsing. The aforementioned microscopic models postulate that the transition to pulsing flow is the outcome of a statistically large number of local pulsatile occurrences in the liquid flow, but make no attempt to describe the nature of the evolution from local pulsing events to bed-scale pulsing. The second approach to describing the hydrodynamic transition is to use a "macroscopic" model. The classic example of this approach is the work of Grosser et al.[12] who predicted the trickle-to-pulse flow transition from a perturbation analysis of a unidirectional, fully developed, volume-averaged and separated two-phase flow Navier-Stokes model. A more recent work based on this analysis is that of Attou and Ferschneider.[13]

To a significant extent, the ability to develop and validate a model for use in predicting the trickle-to-pulse transition will be limited by our ability to measure the transition, and, perhaps, more importantly, to identify unambiguously what we mean by the term "transition". For completeness, a summary of the experimental approaches taken to studying the trickle-to-pulse transition is now given. As discussed earlier, the earliest studies were made by visual inspection of columns with optically transparent walls[2]; such studies were, therefore, inherently limited in their ability to give insight into what was happening in the interior of the bed. An alternative approach, which did reflect the global behavior of the bed, was to use conductance techniques to detect changes in gas-liquid holdup averaged over a cross-section perpendicular to the direction of flow.[15,18,19] This method gives important information about macroscale phenomena occurring during pulsing flow, for example, "pulse" velocities and frequencies. Other nonspatially resolved techniques include pressure probes, and tracer and anemometry/microphone techniques.[11,15] The advent of tomographic techniques to gain insight into the 2- and 3-D behavior of the gas-liquid distribution and flow during trickle-bed operation offers significant opportunities for taking forward our understanding of hydrodynamic transitions in these systems. Tomographic methods previously applied to study two-phase flow under trickle-flow conditions include conductance and capacitance methods,[20-22] optical methods,[23-25] X-ray tomography[26-28] and MRI.[29-31] Of these, only capacitance tomography and MRI have been successfully used to visualize transient flows in trickle-bed reactors. In particular, Reinecke and Mewes[22,32] successfully implemented capacitance tomography to acquire rapid (70 Hz) 2-D information with an in-plane pixel resolution of 3.75 mm $\times$ 3.75 mm, and an axial electrode measurement of 30 mm. They observed that the pulses passing through the column were not liquid slugs of a certain thickness covering the whole cross-section but only liquid-rich bands moving within the bed; estimates of the pulse velocity were also given. With respect to MRI, Sederman and Gladden[29] have shown that MRI can be used to study the 3-D gas-liquid distribution during trickle flow from which direct measurements of liquid holdup and catalyst wetting are obtained. More recently, Lim et al.[30] and Sederman and Gladden[31] reported the use of an ultrafast 2-D MRI technique to investigate the stability of the gas-liquid distribution in the trickle- and pulsing-flow regimes. At the onset of the transition to pulsing flow, local pulsing at the length-scale of the size of the packing elements was observed within the bed. Increasing liquid velocity, at a constant gas velocity caused an increase in the number of these pulses, but it was not possible to investigate in detail the evolution of these local pulsing events through the transition since only 2-D data were acquired. These studies also confirmed the conclusion of Reinecke and Mewes[22,32] that liquid slugs did not cover the entire cross-section of the bed, but merely represented an increase in liquid holdup within sections of the column. Lim et al.[30] extended the application of 2-D MRI studies to perform a preliminary investigation of the absolute stability of the liquid phase under conditions of trickle flow. It was shown that even when the macroscopic gas-liquid distribution is constant, well-defined temporal correlations in local liquid content exist. These data have been interpreted as evidence of liquid films of fluctuating thickness on the surface of the packing elements. Work is ongoing to see the extent to which these instabilities are associated with the formation of the local pore-scale pulsing events which we identify as central to the mechanism of the trickle-to-pulse transition in this article.

This article extends our earlier 2-D studies of the nature of the trickle- to pulse-flow transition by using ultrafast 3-D MRI of the liquid distribution within the bed. By imaging the liquid distribution within a 3-D volume of the bed it is possible to study the spatial evolution of the local pulsing events as a

function of the operating conditions of the reactor. Image analysis techniques are used to quantify the number and size of the local pulsing events so that the evolution of these liquid instabilities within the bed can be followed through the hydrodynamic transition. The following conclusions are drawn from this study:

1. The onset of the transition is identified by the occurrence of local pulsatile events within the bed, suggesting that a "microscopic" mechanism describing the trickle-to-pulse transition is most appropriate. These isolated pulses are typically of size-scale not exceeding that of 2 packing elements within the bed.

2. The local pulsatile events "switch on" and "switch off" within the bed as a function of time. Specific regions of the bed appear to have a high probability of being associated with local pulsatile events. In other regions of the bed local pulsatile events do not occur, suggesting that the structure of the bed determines the location of the local instabilities in the liquid flow.

3. For a constant gas velocity, as liquid velocity is increased, the number of local pulsatile events increases until a maximum number $N_{max}$, is reached. We define the liquid velocity at which $N_{max}$ occurs as the transition point. At higher liquid velocities the pulses grow and merge until the whole bed is characterized by a temporally unsteady liquid distribution.

4. As gas velocity increases so the liquid velocity at which the trickle-to-pulse transition occurs decreases and the value of $N_{max}$ increases. Furthermore, the transition from the state of the bed being characterized by local pulsatile events to that at which the entire bed is associated with unstable liquid distribution occurs over a wider range of liquid velocities at high gas velocities.

5. Considering our experimental data recorded for the bed loaded with cylindrical packing elements and using our objective definition of the transition point we obtained good agreement with the predictions of Blok et al.[15] and Larachi et al.[33], suggesting that our association of the liquid velocity at which $N_{max}$ occurs with the transition point is appropriate. Furthermore, we obtained excellent agreement between our experimental determinations of the transition point for the bed packed with spherical packing elements with the predictions of the model of Ng.[16] This result gives support to our conclusion that the mechanism for the hydrodynamic transition requires formation of local pulsing events, and that the conditions under which the transition occurs are dependent on particle shape.

## Experimental Methods

### *Experimental setup and procedure*

The experimental setup is shown in Figure 1. The experiments were carried out using a 70 cm long trickle-bed column constructed of PTFE with an internal dia. of 43 mm. The column was packed with porous cylindrical alumina pellets of length and dia. 3 mm, and bed voidage ~0.38. The pellets were soaked in deionized water for 24 h prior to the experiment in order to fully prewet the pellets. The packed bed was prepared by loading the column to a height of 10 cm, and then tapping repeatedly to consolidate the packing. This procedure was repeated, each time increasing the height of the packing by 10 cm until the column was full. The bed was then operated in the pulsing-flow regime to further consolidate the bed over a

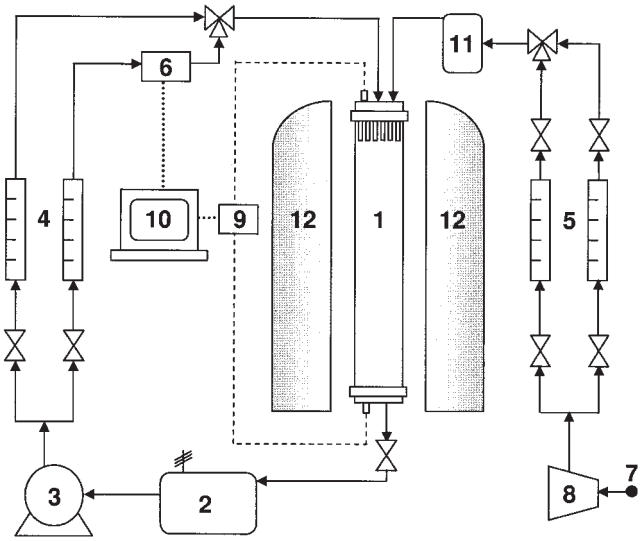


**Figure 1. Flow loop: 1: column; 2: liquid reservoir; 3: liquid gear pump; 4: liquid flow meters; 5: gas flow meters; 6: electronic mass flow measurement and control; 7: compressed air line (6 barg); 8: pressure reducer; 9: pressure transducer; 10: PC; 11: gas saturator; 12: 4.7 T superconducting magnet.**

period of 1.5 h before MRI measurements were acquired. The liquid and gas used were water and air, respectively. The liquid was pumped using a gear pump and its flow rate controlled by an electronic Coriolis mass flow controller (M55C4-AAD-11-K-C from Bronkhorst). The trickle bed was operated under cocurrent downflow conditions. The liquid was fed to the bed through a distributor plate at the top of the PTFE column, and the gas flow was taken from a 6 barg oil-less airline and passed through a variable pressure reducer to 2 barg, after which it was fed through a rotameter and needle valve. The gas entered the top of the column around the outside of the distributor plate. At the base of the column, a single return line returned the liquid-gas mixture to a reservoir where the gas was released to atmosphere. Pressure drop measurements were taken over a length of the packing of 68 cm at time intervals of 0.5 s and logged for a period of 10 min; these measurements were recorded simultaneously with the MRI data.

Experiments were performed for gas superficial velocities $u_G$, of 25, 75, 150, and 300 mm $s^{-1}$ (0.04, 0.09, 0.18 and 0.36 kg $m^{-2}s^{-1}$), and for each of these gas velocities, 27 liquid superficial velocities $u_L$ were studied in the range 0.9 – 13.0 mm $s^{-1}$ (0.9 and 13.0 kg $m^{-2}s^{-1}$). Experiments were performed by setting the gas velocity and then monotonically increasing or decreasing the liquid velocity at the constant gas velocity. Before changing the gas or liquid flow rates to the bed, a standard protocol was followed: (1) Before each of the gas superficial velocities was fixed the bed was operated in the fully developed pulsing regime for 20 min at $u_G = 300$ mm $s^{-1}$ and $u_L = 12.0$ mm $s^{-1}$. (2) Both the gas and liquid flows were then stopped and the bed was allowed to drain for 30 s. The required gas velocity and the lowest liquid velocity were then set simultaneously. Having established the gas and liquid flows, the bed was operated for 15 min at these conditions to

reach steady state before MRI data were acquired. Confirmation of steady state during trickle flow was obtained using two techniques: ultrafast (20 ms/frame) 2-D MRI images and pressure drop measurements. By acquiring successive 2-D images and integrating the signal intensity within each image, it was observed that total signal intensity, corresponding to liquid content within the image slice, reached a constant value in less than 10 min. More detailed study of the individual images confirmed that the spatial distribution of the liquid within the bed was also constant by this time. Simultaneous pressure drop measurements also showed that the pressure drop had converged to a steady value over the same time-scale. (3) After each acquisition, the liquid velocity was stepped up to the next highest liquid velocity, and, once the maximum value had been reached, the liquid flow was then stepped down in the same increments. This procedure was adopted to investigate the presence of any hysteresis in the behavior of the trickle-to-pulse transition. MRI data were acquired from a 3-D volume of dimension 60 mm $\times$ 60 mm $\times$ 60 mm, the center of which was 50 cm below the liquid distributor plate.

A preliminary investigation of the effect of particle shape on the characteristics of the hydrodynamic transition was performed using the 70 cm long bed, packed with alumina spheres of dia. 3 mm. The bed loading procedure was exactly the same as that described earlier for the cylindrical packing elements. For the column packed with spherical packings, five constant gas velocities were studied: 25, 75, 150, 225 and 300 mm $s^{-1}$. The same liquid velocities were studied as for the experiments performed on cylindrical packing elements.

### *MRI*

The $^1$H MRI data were acquired at a frequency of 199.7 MHz on a Bruker Spectrospin DMX 200, 4.7 T magnet with a birdcage coil of length and dia. 6.3 cm, and shielded gradient coils providing a maximum gradient strength of 13.50 G $cm^{-1}$. Two types of images were acquired. First, a high-spatial resolution image of the completely water-saturated bed was acquired using a RARE pulse sequence[34] to provide accurate identification of the position of packing elements within the bed. A spatial resolution of 175 $\mu$m $\times$ 175 $\mu$m $\times$ 175 $\mu$m was obtained using a recycle time of 5 s, an echo time of 7.4 ms, 4 averages and a RARE factor of 32 giving a total acquisition time of 11.5 h. Second, 3-D images of the liquid distribution within the bed for each set of operating conditions were acquired using an ultrafast FLASH pulse sequence[35] with ramped gradients. A bed volume (that is, field-of-view) of 60 mm $\times$ 60 mm $\times$ 60 mm was excited using hard pulses with a pulse of length 7 $\mu$s giving a pulse angle ($\alpha$°) of 5.5° and a gradient-echo time of 0.6 ms. The relatively long gradient-echo time compared to the $T_2^*$ of the intraparticle water, which is approximately 0.3 ms, means that the contribution of the intraparticle water to the signal is negligible, and, therefore, allows us to visualize only the interparticle liquid. Figure 2 shows the pulse sequence used. The data arrays acquired were of size 16 $\times$ 16 $\times$ 32, which, given the field-of-view used, yielded a spatial resolution 3.75 mm $\times$ 3.75 mm $\times$ 1.87 mm; thus, the volume of a single image voxel is approximately that of an individual packing element within the bed. The data acquisition time was 280 ms. 3-D images were acquired in immediate succession, therefore, data were acquired at a rate of 3.6 images per s. Due to hardware limitations only 8 consecutive images could be acquired. For each set of operating conditions of the trickle bed, 6 sets of 8 consecutive images were acquired. As discussed in our earlier article,[36] the FLASH imaging pulse sequence used here provides a robust measure of the liquid distribution (that is, whether or not liquid is present within a given image voxel), but we do not attempt to quantify the liquid holdup from these data.

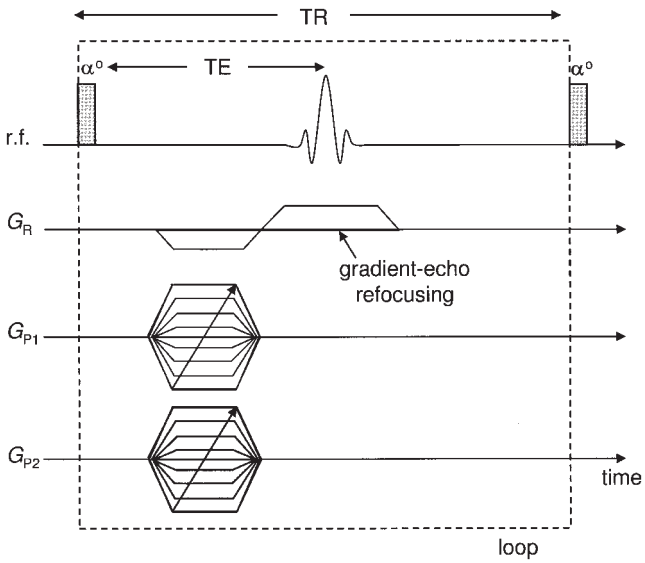


**Figure 2. 3-D FLASH pulse sequence used in all the fast 3-D MRI data acquisitions; TE and TR are the echo time and recycle time, respectively.**

32 points were acquired in the read direction ($G_R$) and 16 points were acquired both in the first ($G_{P1}$) and second ($G_{P2}$) phase directions. $G_R$ is applied in the direction of superficial flow.

### *Data Analysis*

The FLASH images acquired were analyzed as follows. First, 3-D standard deviation maps were calculated from the groups of 8 images acquired within a single experiment. High values of standard deviation identify voxels that are associated with time-varying liquid content. Following calculation of the standard deviation map, the data are binary gated such that only those voxels associated with a value of standard deviation higher than a critical value are identified as being associated with local pulsing regions within the bed. It is only these pulsing regions, which lie above the gating level that are considered in calculating the statistics describing the evolution of the locally pulsing regions through the hydrodynamic transition. Finally, to provide insight as to how local pulsing relates to the structure of the bed the data arrays of the standard deviation map and the image of the bed are superimposed; this is achieved by linearly interpolating the standard deviation maps (spatial resolution: 3.75 mm $\times$ 3.75 mm $\times$ 1.87 mm) to the same resolution as the high-resolution RARE image of the bed (spatial resolution: 175 $\mu$m $\times$ 175 $\mu$m $\times$ 175 $\mu$m).

Details of the analysis procedure are now given. The calculation of the standard deviation ($\sigma$) map has been described for the case of analyzing 2-D data sets in earlier work.[31] In this work the concept of the $\sigma$-map is extended to the analysis of

3-D data sets. The standard deviation of the signal intensity of voxel $i$, $\sigma_i$, for a series of $n$ images ($n = 8$ in this work) is calculated as

$$\sigma_i = \sqrt{\frac{\Sigma(x_i - \bar{x}_i)^2}{n}}$$

where $x_i$ is the signal intensity of voxel $i$ and $\bar{x}_i$ is the average intensity of voxel $i$. Hence, 6 $\sigma$-maps were calculated for each set of operating conditions of the trickle bed. For each 3-D standard deviation map, a mean value ($\sigma_{mean}$) of the standard deviation is calculated from the values comprising the complete map; this parameter acts as a single-value descriptor of the instability of the liquid distribution within the volume of the bed imaged.

To use the 3-D array of information in the standard deviation map, each standard deviation map was binary-gated such that voxels associated with a value of standard deviation lying above the gating value ($\sigma_{crit}$) were considered to be associated with a significantly unstable liquid content (that is, they are identified as locally pulsing regions), whereas those lying below the gating level were considered to have a stable liquid content, and were not considered further in the analysis. Given that the standard deviation of the noise level ($\sigma_{noise}$) in the images was ~0.2, and that the standard deviation of a voxel associated with fully pulsing flow rarely exceeds 2.0, a value of $\sigma_{crit}$ equal to 1.0 was used in the analyses reported here. This is equivalent to taking a gating level of $5\sigma_{noise}$ and is, therefore, consistent with the analyses of 2-D data reported elsewhere.[30] All analyses reported here were also performed with gating levels in the range $0.8 < \sigma_{crit} < 1.4$. While the absolute number of isolated pulsing regions that were identified decreased slightly as the gating level increased, the trends in the data presented, including the liquid velocity at which the maximum number of isolated liquid pulses occurs, remained the same.

Following gating, the 3-D standard deviation maps comprise values of only 1 and 0 indicating voxels associated with unstable and stable gas-liquid content, respectively. These gated data arrays were then analyzed using an in-house algorithm to identify the number and size (in terms of number of voxels) of clusters of voxels associated with an unstable gas-liquid distribution. The fraction of the total bed void space associated with unstable gas-liquid distribution is also obtained. A "cluster" of voxels comprising a local pulsing region is defined as a group of 1-value voxels connected to each other by at least one corner. This choice of connectivity criterion is rationalised by the fact that if we consider the 3-D interparticle space (void space) of the bed to be comprised of a 3-D network of pores and constrictions, it is most likely that if voxels either side of a constriction are associated with locally pulsing flow, then the two pulsing regions are not independent of one another — hence, they are assigned to the same cluster. An alternative choice of connectivity criterion is that "pulsing" voxels belong to the same cluster only if they share at least an edge. All results presented here are robust to this change in criterion, although the absolute numbers of cluster and their sizes will differ. The liquid velocities at which the onset of pulsing occurs and the transition point itself do not change. All data were analyzed over a bed height of 45 mm.

## Results

The results are reported as follows. First, an example of the analysis of the evolution of local pulsing behavior is presented as a function of liquid velocity. Data for the case of a constant gas velocity of 300 mm $s^{-1}$ are shown. At this point an objective definition of the transition point is proposed. The evolution of the number and size of local pulsing events as a function of liquid velocity is also compared with the behavior of the pressure drop readings along the length of the bed. Second, the effect of the gas velocity on the nature of the trickle-to-pulse transition is presented. Third, the sensitivity of the analysis to the location of the imaging volume along the length of the column is reported. Finally, for each of the four gas velocities studied, the liquid velocity at which the maximum number of isolated pulses is observed is compared with the predictions of earlier workers. At this point the data obtained for the bed packed with spherical packing elements is also presented. In Figures 3–5 individual standard deviation maps are shown which have been calculated from a single series of 8 consecutive 3-D images. The statistical data shown in Figures 6–10 are calculated from the 6 standard deviation maps obtained form the 6 separate experiments performed at each operating condition.

### *Trickle-to-pulse transition for $u_G = 300$ mm $s^{-1}$*

Figures 3 and 4 show two different views of the combined 3-D structural image of the bed, and the standard deviation maps for a constant gas superficial velocity of 300 mm $s^{-1}$. Data are shown for 8 liquid superficial velocities spanning the trickle-to-pulse transition increasing from 3.9 mm $s^{-1}$ to 12.2 mm $s^{-1}$. In both figures the cylindrical pellets are depicted in black, and the interparticle space was assigned a range of colors between blue and red (as indicated by the legend) depending on the value of the standard deviation of the signal intensity in that region of the bed observed between successive images, that is, the stability of the gas-liquid distribution in that region. Large fluctuations in the liquid distributions, corresponding to values of the standard deviation equal to or greater than 1.0 are depicted in red. It is only the regions identified as red that are used in the analysis of the local pulsing clusters in subsequent analysis.

Figure 3 shows the evolution of the liquid instabilities for increasing liquid velocities in a cross-section of the column perpendicular to the direction of flow; a bed height of only 9 mm is shown. For liquid superficial velocities ($u_L$) below 5.2 mm $s^{-1}$ the gas-liquid distribution is constant, as expected for trickle-flow conditions, with most of the cross-section showing values of the standard deviation between 0.2 and 0.5 (in blue and green). In the section of the bed shown, localized regions of liquid instability occurring over a length scale of order the size of a packing element are observed at values of $u_L$ as low as 4.6 mm $s^{-1}$ (Figure 3b). At increasing values of $u_L$ these regions increase in number, grow and then merge with each other, eventually covering most of the cross-section. The evolution of the pulsing events observed in the 3-D images acquired at 280 ms per frame is consistent with the 2-D data reported earlier[30,31] which were acquired at a faster rate (20 ms per frame). The time scales over which the local pulses occurred, as determined in the 2-D study, were typically 0.4 – 10 s, and, therefore, both the 2- and 3-D acquisitions will be

sensitive to the local pulsing events, which are the focus of this article. However, the 3-D data acquisition will not be sensitive to any rapidly changing liquid content that averages to a similar value in successive image acquisitions. Therefore, the 3-D experiments are unlikely to be able to detect the higher frequency fluctuations (<0.1 s) in liquid content that occur during trickle flow that have been observed in 2-D studies, and which have tentatively been assigned to fluctuations in the thickness of surface wet layers on the packing elements prior to formation of the local pulsing events.[30]

Figure 4 shows the evolution of the liquid instabilities in a section of the bed of height 40 mm. This cut through the 3-D dataset allows us to visualize the spatial extent of the local pulses. When the local pulses are first formed they have a volume no greater than 2 $V_p$, where $V_p$ corresponds to the volume of one packing element ($\sim$0.02 cm$^3$). The more quantitative analysis, to be presented later, reveals that the maximum number of local (isolated) pulsing regions ($N_{max}$) occurred at a $u_L$ of 6.1 mm s$^{-1}$ (Figure 4d). At liquid velocities greater than this, the regions of unstable liquid content start to merge and form larger pulsing clusters with volumes in the range 5 – 10 $V_p$, eventually occupying the whole volume of the column at the highest liquid velocities studied (Figure 4h).

Figure 5 shows six standard deviation maps presented as in Figures 3 and 4, but in this case all maps are shown for a value of $u_L$ of 6.1 mm s$^{-1}$. The height of the bed shown is 34 mm. Each standard deviation map is calculated from a separate series of 8 images of the gas-liquid distribution within the bed; the total data acquisition time for all 8 images in a given series was 2.24 s. In Figure 5 we clearly observe that at this value of $u_L$, which corresponds to that at which the maximum number of local pulsing events occurs, the local pulses "switch on" and "switch off" as a function of time, as seen in the highlighted regions A and B. Other regions of the bed (region C) are identified in which no isolated pulses are observed. Thus, we suggest that some regions of the bed are more likely to be associated with a stable or unstable liquid distribution, suggesting that the structure of the bed plays a role in determining the position of local pulsing events.

Figure 6 shows the results of the analysis of the binary-gated standard deviation maps. Figure 6a shows both the average number of individual pulses and the total pulsing volume as a function of liquid velocity. Both these sets of data show average values calculated from the 6 standard deviation maps, each of which was calculated from a series of 8 images of gas-liquid distribution. It is seen that at low values of $u_L$ there are no pulsing (that is, unstable) regions in the volume imaged. As the liquid velocity is increased, the number of pulsing regions increases until it reaches a clear maximum ($N_{max}$) of 28 at a liquid velocity of 6.1 mm s$^{-1}$. This characteristic peak shape describing the evolution of the number of isolated liquid pulses as a function of liquid velocity was observed in all experiments and, therefore, we have taken the liquid velocity at which $N_{max}$ occurs to be an objective definition of the transition point between trickle and pulsing flow, and will now refer to the liquid velocity at which this $N_{max}$ occurs as $u_{LT}$. For $u_L > u_{LT}$, the number of independent regions associated with unstable liquid distribution decreases until it reaches 1 or 2. Combining this information with the total pulsing volume data, we observe that the volume of the first liquid pulses is very small. Considering the data from all 8 standard deviation maps, the first pulses are observed at a $u_L$ of 3.0 mm s$^{-1}$ and have an average volume of 2.17 $V_p$. The behavior of the average number of liquid pulses and the associated total pulsing volume show the same characteristics for each of the 4 values of $u_G$ investigated. Figure 6b shows how the number of pulsing regions relates to the standard deviation of the pressure drop measurement taken over the length of the column. A sharp increase in the standard deviation of the pressure drop measurements occurs near $u_{LT}$. However, this transition is not as clearly defined as that identified by the peak in the number of liquid pulses.

Figure 7 focuses on the statistical evolution of the individual pulsing regions, and their sizes up to $u_L = u_{LT}$ (= 6.1 mm s$^{-1}$). Figure 7a shows the total number of pulses of sizes between 1–30 $V_p$ occurring at $u_L$ = 4.6 mm s$^{-1}$ at which point isolated pulses are only just beginning to form. At $u_L$ = 5.7 mm s$^{-1}$ (Figure 7c) 52 regions had volumes of 1-2 $V_p$, while only 14 pulsing regions presented the second most commonly occurring volume size (2–4 $V_p$). Figures 7(b–d) show that as the liquid flow rate was increased up to $u_{LT}$ the number of pulsing regions increased and, furthermore, the majority of the pulsing regions remain characterized by small volumes. For all four values of $u_L$ shown in Figure 7, the majority of individual pulses had volumes of 1-2 $V_p$. For completeness, Figure 8 shows how both the total pulsing volume and the average standard deviation value calculated from the 3-D $\sigma$-maps have the same form as a function of liquid velocity, with their point of inflection occurring near $u_{LT}$.

### *Effect of gas velocity*

The effect of changing the gas velocity on the nature of the hydrodynamic transition is shown in Figure 9. As observed in Figure 9a, the value of $N_{max}$ decreases and the value of $u_{LT}$ shifts to higher values, with decreasing $u_G$. For example, at $u_G$ = 300 mm s$^{-1}$ the values of $N_{max}$ and $u_{LT}$ were 27.5 and 6.1 mm s$^{-1}$, respectively, while at $u_G$ = 25 mm s$^{-1}$ $N_{max}$ took the value of 12.5 and $u_{LT}$ occurred at a liquid velocity of 8.7 mm s$^{-1}$. The observation that the hydrodynamic transition occurs at lower values of liquid velocity as gas velocity increases is in agreement with previous experimental observations[14,37,38] and theoretical predictions[12,15,16]. Figure 9b shows the fraction of the bed that is associated with pulsing liquid as a function of $u_L$. These data suggest that the merging of isolated liquid pulses such that the bed moves into the pulsing regime, occurs more rapidly with decreasing $u_G$. Figure 10a,b shows the evolution of the number of isolated pulses as a function of $u_L$ for gas velocities of 75 and 300 mm s$^{-1}$. Data are shown for both increasing and decreasing liquid velocity, and it is clearly seen that no hysteresis is observed. These data are consistent with the pressure drop readings recorded at the same time, which also showed no hysteresis. The data shown in Figures 9 and 10 also show that the isolated pulses that exist prior to the transition are small, indeed $\sim$70% being less than 2$V_p$ for $u_L \leq u_{LT}$. These data also suggest that higher gas velocities result in isolated pulses of larger size.

### *Effect of the location of the image volume*

The objective of this part of the study was two-fold. First, to confirm that the data presented are not dominated by the fact that the image volume is located only $\sim$20 cm from the bottom

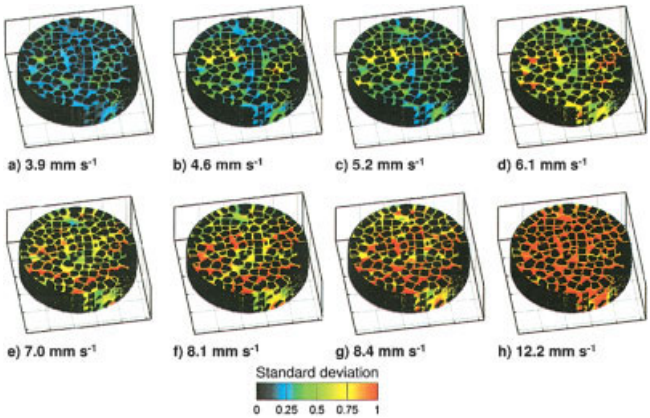


**Figure 3. Evolution of local pulsing events across the bed as a function of liquid velocity.**

3-D standard deviation maps calculated from data acquired with the bed operating at a constant gas velocity of 300 mm $s^{-1}$ for liquid velocities in the range 3.9 – 12.2 mm $s^{-1}$ are shown. The height of the bed section is 9 mm. The standard deviation maps are shown combined with the 3-D RARE image of the internal structure of the bed. The standard deviation maps (3.75 mm × 3.75 mm × 1.87 mm) have been linearly interpolated to the same resolution as the RARE image (175 $\mu$m × 175 $\mu$m × 175 $\mu$m) to provide a better insight to how local pulsing relates to the structure of the bed. The direction of superficial flow is perpendicular to the cross-section of the bed shown. Regions of unstable liquid content, that is, local pulsing regions) are identified as red. The same color scale is used in Figures 4 and 5.

of the bed. Second, to investigate the effect of moving the image volume to different distances from the entrance to the bed. A bed of length 2.20 m was loaded with the same packing material using the same procedure as described previously for the shorter bed. For a constant gas velocity of 75 mm $s^{-1}$, 27 liquid superficial velocities, $u_L$, were studied in the range 0.9 – 13.0 mm $s^{-1}$ for each of two image volume locations; namely

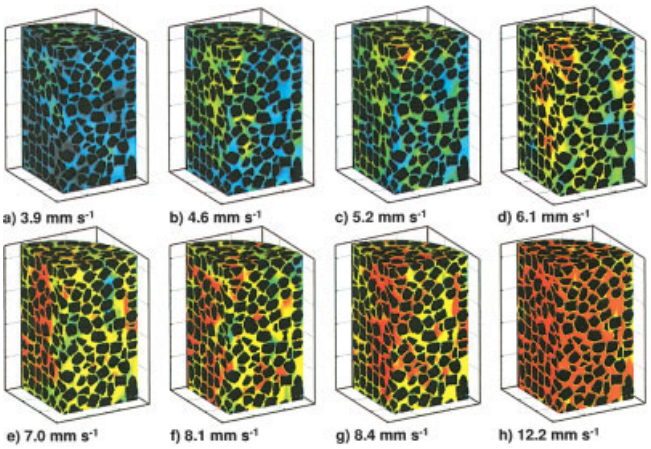


**Figure 4. Evolution of local pulsing events along the length of the bed as a function of liquid velocity.**

3-D standard deviation maps of a vertical section, of height 40 mm, through the bed are shown. The bed is operating at a constant gas velocity of 300 mm $s^{-1}$ for liquid velocities in the range 3.9 – 12.2 mm $s^{-1}$. As in Figure 3, the standard deviation maps have been linearly interpolated to the same resolution as the RARE image (175 $\mu$m × 175 $\mu$m × 175 $\mu$m).

with the center of the image volume being 1.0 m and 2.0 m below the distributor plate. These data were then compared with those obtained from the short column in which the data were acquired with the center of the image volume 0.5 m below the distributor plate. It follows that if all three data sets give consistent values of the liquid velocity at which the hydrodynamic transition occurs, $u_{LT}$, then we can conclude that the characteristics of the hydrodynamic transition are the same throughout the length of the column (certainly to within 20 cm of the column exit). Alternatively, if the MRI data for the short column agree with the data recorded 2.0 m below the distributor in the long column, but are significantly different to the data obtained at 1 m below the distributor in the long column, then it may be that the data we report for the short column are dominated by exit effects.

The values of $u_{LT}$ at distances of 1.0 and 2.0 m from the entrance to the bed of length 2.2 m, were found to be 7.2 and 6.6 mm $s^{-1}$, respectively. These values compare with a value of $u_{LT}$ = 7.5 mm $s^{-1}$ for the shorter column used in the earlier studies for which the imaging volume was 0.5 m from the top the bed and 0.2 m from the bottom of the bed. From these data it is clear that the value of $u_{LT}$ scales linearly with distance from the top of the bed, and does not correlate with distance from the bottom of the bed. Thus, we can conclude that the data reported in this article are not dominated by the location of the imaging volume in the 70 cm long column being 20 cm from the bottom of the bed. Furthermore, our data are in agreement with the results of earlier workers who reported that the value of liquid velocity at which the hydrodynamic transition occurs decreases with increasing distance from the distributor.[21,23]

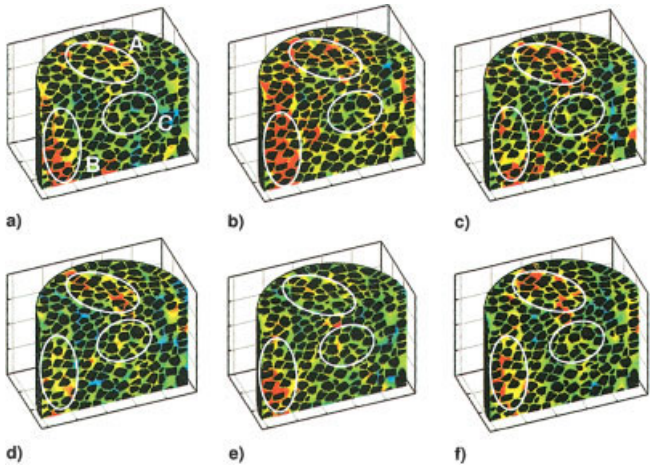


**Figure 5. Time-dependent behavior of local pulsing events.**

3-D standard deviation maps combined with a RARE image of the bed structure are shown for a bed height of 34 mm. All maps were calculated from 3-D MRI datasets acquired with the bed operating under the same conditions with gas and liquid velocities being 300 and 6.1 mm $s^{-1}$, respectively. The data for each map was acquired in 2.24 s and the time interval between the data acquisition for each of the standard deviation maps was 2 s. Regions A and B identify volumes within the bed at which local pulses are observed; these local pulses "switch on" and "switch off" as a function of time. There also appear to be regions in the bed, such as that identified as C, in which local pulses are not observed suggesting that the local structure of the bed plays a role in determining the spatial location of the local pulsing events.

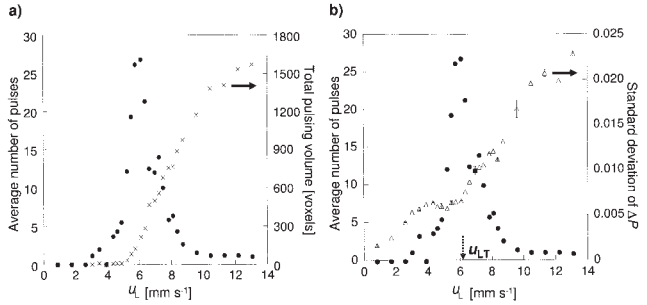


**Figure 6. Analysis of the 3-D standard deviation maps calculated from data acquired with the bed operating at a constant gas velocity of 300 mm s$^{-1}$.**

(a) The average number of independent liquid pulses identified at each liquid velocity (●), and the total number of voxels within the 3-D image associated with liquid pulses (×). (b) The average number of pulsing regions (●) in the image volume and the standard deviation of the pressure drop readings recorded along the length of the column (Δ). The average standard deviation in the pressure drop was calculated from data recorded at 0.5 s intervals over a period of 10 min. One-sigma error bars are shown.

### *Comparison with theoretical models*

Figure 11 shows a summary of the experimental results obtained. For each of the gas velocities studied the value of $u_{LT}$ is shown. The values of $u_{LT}$ obtained for the experiments

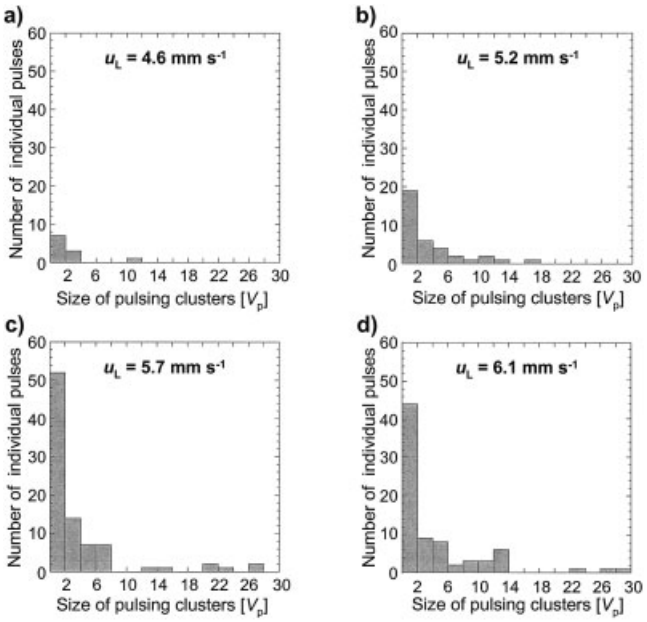


**Figure 7. Histograms showing the number of local pulses of a given size where the unit of size is $V_p$, the volume of an individual packing element within the bed (0.02 cm$^3$).**

The data for these histograms were obtained from 6 standard deviation maps. Data are shown for the bed operating at a constant gas velocity of 300 mm s$^{-1}$ and at liquid velocities in the range 4.6 – 6.1 mm s$^{-1}$. For clarity data are shown only up to local pulse volumes of 30 $V_p$. In addition to the data shown at $u_L$ = 5.7 mm s$^{-1}$ single pulses of volume 34, 37, 47, 57 and 65 $V_p$ were observed. At $u_L$ = 6.1 mm s$^{-1}$ single pulses of volume 32, 38, 70, 88 and 96 $V_p$, and two pulses of volume 84 $V_p$ were also observed.

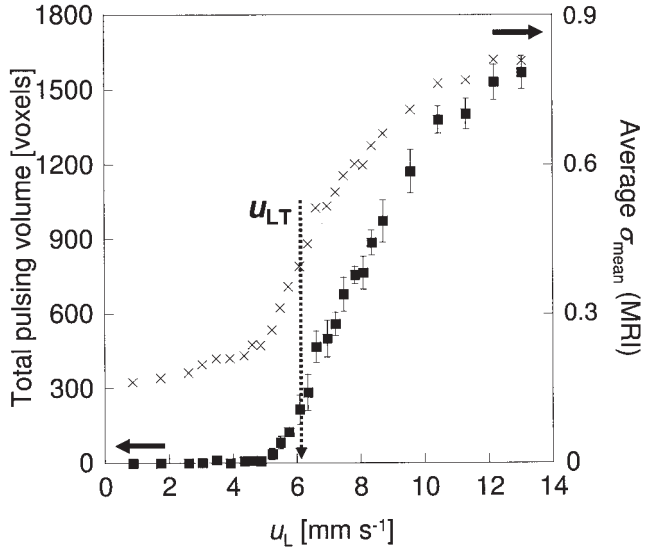


**Figure 8. The evolution of the total number of voxels associated with liquid pulses (×) is compared with the average of the 3-D standard deviation values ($\sigma_{mean}$) calculated from 6 individual standard deviation maps (■); one-sigma error bars are shown.**

Data are shown for the bed operating at a constant gas velocity of 300 mm s$^{-1}$. The one-sigma error bars on the total pulsing volume data are no larger than the dimensions of the symbols used.

performed with the column packed with spherical packing elements are also presented. It is clearly seen that the value of $u_{LT}$ shifts to higher values of $u_L$ as we switch from cylindrical to spherical packing elements. The effect of the size and shape of the packing elements on the nature of the hydrodynamic

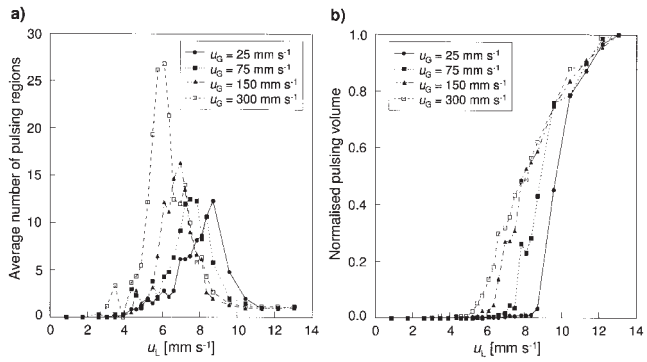


**Figure 9. Effect of gas velocity on the characteristics of the trickle-to-pulse transition.**

(a) Number of local pulsing regions identified as a function of liquid velocity for four different gas velocities: 25, 75, 150 and 300 mm s$^{-1}$. For each value of gas velocity a peak in the number of local pulsing regions, $N_{max}$, is clearly identified. The liquid velocity at which $N_{max}$ occurs decreases with increasing gas velocity. (b) The volume of the bed associated with local pulsing events for the same operating conditions as shown in (a). These data are derived from the absolute number of voxels associated with unstable liquid content. The data are normalized because the maximum number of voxels associated with unstable liquid content depends on the value of $u_G$ considered.

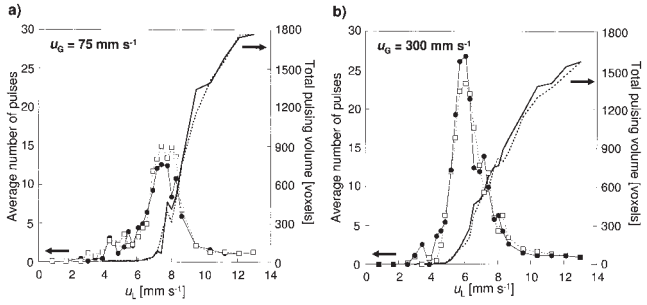


**Figure 10. The average number of local pulses and total number of voxels associated with individual liquid pulses for a constant gas velocity of (a) 75 mm s$^{-1}$ and (b) 300 mm s$^{-1}$.**

Data are shown for increasing and decreasing liquid velocity. No hysteresis is observed. The average number of pulses are shown as (●) and (□) for increasing and decreasing liquid velocity, respectively. The total pulsing volume is also shown for increasing (——) and decreasing (·····) liquid velocity.

transition is the subject of ongoing work and will not be discussed here. These preliminary data are shown purely in the context of discussing the performance of the various empirical and theoretical predictions of the liquid velocity at which the hydrodynamic transition occurs. The particular models considered are the empirical models of Blok et al.[15] and Larachi et al.[7,33], and the theoretical models of Ng[16] and Grosser et al.[12]. The model of Ng[16] is based on the "microscopic" approach, while that of Grosser et al.[12] is a "macroscopic" model.

A sensitivity analysis of the predictions of the various models to their input parameters was performed because the conditions used as input to these models when originally reported did not necessarily correspond to those used in our experiments. The parameters considered were gas density, bed voidage, and in the case of the model of Grosser et al., the Ergun constants. The sensitivity to gas density was considered by comparing values of gas density corresponding to an operating pressure of 2 bar, as used in our experiments, with that corresponding to operation at 1 bar. The predictions of the model of Larachi et al.[33] were found to be insensitive to this change in gas pressure. In contrast, the models of Blok et al., Larachi et al.[7], Ng and Grosser et al. were sensitive to gas pressure. The most sensitive of these was the model of Grosser et al. for which the value of liquid velocity at which the transition occurred decreased by up to 25% in moving from operation at 2 bar to 1 bar. The model of Ng was more sensitive to gas pressure at high-gas velocities and predicted an increase of ~17% in the liquid velocity at which the transition occurred for a gas velocity of 300 mm s$^{-1}$, when the gas pressure was decreased to 1 bar. The same variation in gas pressure modified the values predicted by the models of Blok et al. and Larachi et al.[7] by less than 6% for all gas velocities considered. Sensitivity to bed voidage was considered as follows. The value of the bed voidage determined for the column packed with cylindrical packing elements was 0.38; this value was obtained from the high-resolution 3-D magnetic resonance image of the bed, and it is in agreement with values reported in the literature for similar packings.[3,4] The predictions of the models, except for that of Larachi et al.[33] which does not have bed voidage as an input parameter, were considered for values of bed voidage in the range 0.38 ± 0.02. Increasing the bed voidage, increased the value of the liquid velocity at which the transition was predicted to occur. For the models of Ng, Blok et al. and Larachi et al.[7] the predicted transition point was changed by less than 5%. The model of Grosser et al. was more sensitive and was found to vary by up to 28%. However, the model of Grosser et al. was relatively insensitive to the values of the Ergun constants. In Figure 11, the predictions of the model are shown for models of the Ergun constants A and B of 180 and 1.8. Using values of A and B of 300 and 2.0, respectively, increased the liquid velocity at which the transition was predicted to occur by less than 5%. Given the results of this sensitivity analysis we are confident that the general conclusions we draw in comparing the predictions of the models to the results of our experimental study are valid.

With reference to Figure 11, we see that there is quite good agreement between our values of $u_{LT}$ for cylindrical packing elements and the liquid velocities at which the transition occurs as predicted by the models of Blok et al. and Larachi et al.[33]. This might be expected due to the fact that these two empirical models were based on experimental studies in which a signif-

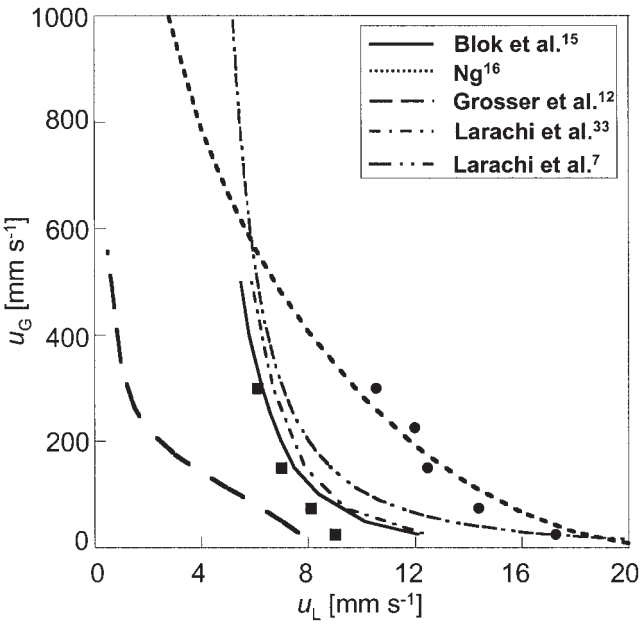


**Figure 11. Comparison of the results of the analysis of the 3-D MRI data with the predictions of empirical correlations and theoretical analysis.**

The values of liquid velocity at which $N_{max}$ occurs for cylindrical (■) and spherical (●) packing elements are shown. The predictions of the transition point based on the earlier studies of Blok et al.[15], Ng,[16] Grosser et al.[12], Larachi et al.[7,33] are also shown. The parameters used in the various models are: internal column column dia. = 0.043 m; diameter of packing element = 0.003 m; bed voidage = 0.38; Ergun constants: A = $E_1$ = 180 and B = $E_2$ = 1.8; self-diffusion coefficient of air = $1.40 \times 10^{-5}$ m$^2$ s$^{-1}$; self-diffusion coefficient of water = $2.00 \times 10^{-9}$ m$^2$ s$^{-1}$; sphericity factor = 1; air-water surface tension = 0.0728 N m$^{-1}$; gas density = 2.32 kg m$^{-3}$; liquid density = 998 kg m$^{-3}$; gas dynamic viscosity = $1.85 \times 10^{-5}$ Pa s; liquid dynamic viscosity = $1.00 \times 10^{-3}$ Pa s. Fluid properties are given at 293 K and 2 bar, corresponding to the conditions used in the MRI experiments.

icant number of the systems studied considered air/water cocurrent downflow in columns operating at atmospheric pressure. Furthermore, the majority of the packing elements used were cylinders or Raschig rings of similar size and aspect ratio to those studied in this work. This good agreement suggests that the association of the transition point with the liquid velocity at which the maximum number of isolated liquid pulses occurs is appropriate. The trend predicted by the neural network model of Larachi et al.[7] also shows reasonable agreement with our experimental results; this model is based on data for columns packed with a wider range of packing elements and column operating conditions than the model of Larachi et al.[33]. All of the aforementioned models over-predict the liquid velocity at which the transition occurs relative to our determination of $u_{LT}$. The extent of the disagreement between our experimental data, and the model predictions increases with decrease in gas velocity. The macroscopic model of Grosser et al.[12] predicted the transition to occur at values of $u_L$ significantly lower than the values of $u_{LT}$ determined from our MRI data. However, we note that the values predicted by Grosser at al.[12] are more consistent with the liquid velocities at which the onset of pulsing occurs as identified from the data shown in Figure 9a.

From Figure 11 it is also seen that the microscopic model of Ng[16], which was developed for packing elements of spherical geometry, gives excellent agreement with our experimental data. Of course, such good agreement may be fortuitous, and, therefore, the influence of the shape and size of packing elements on the nature of the trickle-to-pulse transition (for example, values of $u_{LT}$ and $N_{max}$) is the subject of ongoing work. Furthermore, we are also considering the interpretation of these MRI data in the light of mesoscale transition models, such as the discrete cell model,[39] and the cell model for structured packings suggested by Mewes et al.[40].

## Conclusions

3-D ultrafast MRI has been used to study the mechanism of the transition from trickle-to-pulsing flow for the first time. The results confirm that the transition to pulsing flow is initiated by local pulsing events of a size-scale typical of the packing elements contained within the column. 3-D MRI allows us to explore the 3-D evolution of the local pulses as the system moves through the trickle-to-pulse transition as a function of liquid velocity for a constant gas velocity. As liquid velocity is increased, the number of isolated liquid pulses increases until a maximum number is reached. The liquid velocity at which the peak in the number distribution of isolated liquid pulses occurs is very clearly defined and, hence, we define this liquid velocity as the transition point. At liquid velocities above the transition point, the pulses grow and merge until the whole bed is characterized by a temporally unsteady liquid distribution. 3-D MRI allows us to estimate the size of the local pulses as the system moves through the trickle-to-pulse transition.

The effect of gas velocity on the hydrodynamic transition has also been studied. As gas velocity increases, so the liquid velocity at which the transition occurs decreases, and the transition from the state of small isolated pulses to the fully pulsing state occurs over a wider range of liquid velocities. The number of isolated pulses existing at the transition point also increases with increasing gas velocity.

The 3-D time-resolved images of liquid distribution within the bed provide strong evidence that the mechanism of the trickle-to-pulse transition in fixed-bed reactors is best described by a "microscopic" or "pore-scale" approach. Comparison with the predictions of existing correlations and theoretical approaches suggests that (1) our definition of the transition point is consistent with that identified by earlier workers using other experimental approaches, and (2) our observations are consistent with the assumptions and predictions of Ng[16] who used a microscopic approach in considering the hydrodynamic transition to be initiated by liquid bridges forming across adjacent packing elements.

## Acknowledgments

We acknowledge the EPSRC, the Cambridge European Trust, the Isaac Newton Trust and Johnson Matthey p.l.c. for financial support of this work.

## Literature Cited

1. Al-Dahhan MH, Larachi F, Dudukovic MP, Laurent A. High-pressure trickle-bed reactors: A review. *Ind Eng Chem Res.* 1997;36:3292-3314.
2. Gianetto A, Baldi A, Specchia V, Sicardi S. Hydrodynamics and solid-liquid contacting effectiveness in trickle-bed reactors. *AIChE J.* 1978;24:1087-1104.
3. Specchia V, Baldi G. Pressure drop and liquid holdup for two phase concurrent flow in packed beds. *Chem Eng Sci.* 1977;32:515-523.
4. Holub RA, Duduković MP, Ramachandran PA. Pressure drop, liquid holdup and flow regime transition in trickle flow. *AIChE J.* 1993;39:302-321.
5. Iliuta I, Ortiz-Arroyo A, Larachi F, Grandjean BPA, Wild G. Hydrodynamics and mass transfer in trickle bed reactors: an overview. *Chem Eng Sci.* 1999;54:5329-5337.
6. Wu R, McCready J, Varma A. Influence of mass transfer coefficient fluctuation frequency on performance of three-phase packed-bed reactors. *Chem Eng Sci.* 1995;50:3333-3344.
7. Larachi F, Iliuta I, Chen M, Grandjean BPA. Onset of pulsing in trickle beds: evaluation of current tools and state-of-the-art correlation. *Can J Chem Eng.* 1999; 77:751-765.
8. Saroha AK, Nigam KDP. Trickle bed reactors. *Rev Chem Eng.* 1996;12:207-347.
9. Dudukovic MP, Larachi F, Mills PL. Multiphase reactors - revisited. *Chem Eng Sci.* 1999;54:1975-1995.
10. Sundaresan S. Modelling the hydrodynamics of multiphase flow reactors: Current status and challenges. *AIChE J.* 2000;46:1102-1105.
11. Sicardi SH, Gerhard H, Hoffmann, H. Flow regime transition in trickle-bed reactors. *Chem Eng J.* 1979;18:251-253.
12. Grosser K, Carbonell RG, Sundaresan S. Onset of pulsing in two-phase cocurrent downflow through a packed bed. *AIChE J.* 1988;34:1850-1860.
13. Attou A, Ferschneider G. Two-fluid hydrodynamic model for the transition between trickle and pulse flow in a cocurrent gas-liquid packed-bed reactor. *Chem Eng Sci.* 2000;55:491-511.
14. Charpentier JC, Favier M. Some liquid holdup experimental data in trickle-bed reactors for foaming and non-foaming hydrocarbons. *AIChE J.* 1975;21:1213-1218.
15. Blok JR, Varkevisser J, Drinkenburg AAH. Transition to pulsing flow, holdup and pressure drop in packed columns with cocurrent gas-liquid downflow. *Chem Eng Sci.* 1983;38:687-699.
16. Ng KM. A model for flow regime transitions in cocurrent downflow trickle-bed reactors.. *AIChE J.* 1986;32:114-122.
17. Kapitza PL. Wave flow of thin viscous fluid layers. *Zhurn Eksper Teor Fiz.* 1948;18:3-28.
18. Tsochatzidis NA, Karabelas AJ. Properties of a pulsing flow in a trickle bed. *AIChE J.* 1995;41:2371-2382.
19. Boelhouwer JG, Piepers HW, Drinkenburg AAH. Nature and characteristics of pulsing flow in trickle-bed reactors. *Chem Eng Sci.* 2002;5:4865-4876.
20. Helwick JA, Dilon PO, McCready MJ. Time-varying behaviour of

cocurrent gas-liquid flows in packed-beds. *Chem Eng Sci.* 1992;47: 33249-3256.
21. Krieg DA, Helwick JA, Dillon PO, McCready MJ. Origin of disturbances in cocurrent gas-liquid packed-bed flows. *AIChE J.* 1995;41: 1653-1666.
22. Reinecke N, Mewes D. Investigation of the two-phase flow in trickle-bed reactors using capacitance tomography. *Chem Eng Sci.* 1997;52: 2111-2127.
23. Melli TR, de Santos JM, Kolb WB, Scriven LE. Cocurrent downflow in networks of passages - microscale roots of macroscale flow regimes. *Ind Eng Chem Res.* 1990;29:2367-2379.
24. Kolb WB, Melli TR, de Santos JM, Scriven LE. Cocurrent downflow in packed beds. Flow regimes and their acoustic signals. *Ind Eng Chem Res.* 1990;29:2380-2389.
25. Tsochatzidis NA, Karabelas AJ. Experiments in trickle beds at the microscale and macroscale - flow characterization and onset of pulsing. *Ind Eng Chem Res.* 1994;33:1299-1309.
26. Kantzas A. Computation of holdups in fluidized and trickle beds by computer-assisted tomography. *AIChE J.* 1994;40:1254-1261.
27. Toye D, Marchot P, Crine M, L'Homme G. Analysis of liquid flow distribution in trickling flow reactor using computer-assisted X-ray tomography. *Chem Eng Res Des.* 1995;73:258-262.
28. Toye D, Marchot P, Crine M, L'Homme G. Modelling of multiphase flow in packed beds by computer-assisted X-ray tomography. *Meas Sci Technol.* 1996;7:436-443.
29. Sederman AJ, Gladden LF. Magnetic resonance imaging as a quantitative probe of gas-liquid distribution and wetting efficiency in trickle-bed reactors. *Chem Eng Sci*. 2001;56:2615-2628.
30. Lim MHM, Sederman AJ, Gladden LF, Stitt, EH. New insights to trickle and pulse flow hydrodynamics in trickle-bed reactors using MRI. *Chem Eng Sci.* 2004;59:5403-5410.
31. Sederman AJ, Gladden LF. Transition to pulsing flow in trickle-bed reactors using MRI. *AIChE J.* 2005;51:615-621.
32. Reinecke N, Mewes D. Tomographic imaging of trickle-bed reactors. *Chem Eng Sci.* 1996;51:2131-2138.
33. Larachi F, Laurent A, Wild G, Midoux N. Effet de la presion sur la transition ruisselant-pulsé dans les réacteurs catalytiques à lit fixe arrosé. *Can J Chem Eng.* 1993;71:319-321.
34. Hennig J, Nauerth A, Friedburg H. RARE imaging-a fast imaging method for clinical MR. *Magn Reson Med.* 1986;3:823-833.
35. Haase A, Frahm J, Matthaei D, Hanicke W, Merboldt KD. Flash imaging - Rapid NMR imaging using low flip-angle pulses. *AIChE J.* 1986;67:258-266.
36. Gladden LF, Alexander P, Britton MM, Mantle MD, Sederman AJ, Yuen EHL. *In situ* magnetic resonance measurement of conversion, hydrodynamics and mass transfer during single- and two-phase flow in fixed-bed reactors. *Magn Reson Imaging*. 2003;21:213-219.
37. Chou TS, Worley FL, Luss Jr D. Transition to pulsed flow in mixed-phase cocurrent downflow through a fixed bed. *Ind Eng Chem.* 1977; 16:424-427.
38. Sai PST, Varma YBG. Flow pattern of the phases and liquid saturation in gas-liquid cocurrent downflow through packed beds. *Can J Chem Eng.* 1988;66:353-360.
39. Jiang Y, Khadilkar MR, Al-Dahhan MH, Dudukovic MP. Two-phase flow distribution in 2D trickle-bed reactors. *Chem Eng Sci.* 1999;54: 2409-2419.
40. Mewes D, Loser T, Millies M. Modelling of two-phase flow in packings and monoliths. *Chem Eng Sci.* 1999;54:4729-4747.

*Manuscript received Jun. 6, 2005, and revision received Oct. 2, 2005.*